Nano Energy 149 (2026) 111729

Contents lists available at ScienceDirect

Nano Energy

journal homepage: www.elsevier.com/locate/nanoen

Multifunctional ultra-low voltage sweat-activated battery using piezo-ionic hydrogel

Mustehsan Beg [1], Vishnu Sam [1], Jithin Kanathedath, Prasutha Rani Markapudi, Keith M. Alcock, Keng Goh, Hongnian Yu, Libu Manjakkal [*]

School of Computing and Engineering & the Built Environment Edinburgh Napier University, Merchiston Campus, Edinburgh EH10 5DT, UK

ARTICLE INFO

Keywords:
Wearable energy storage
Sweat
Piezo-ionic hydrogel
Fabric battery
Energy generator

ABSTRACT

Optimising ultra-low voltage with high capacity in batteries presents a challenge for emerging applications, such as wearable technology. In this study, we developed a multifunctional ultra-low voltage, sweat-activated fabric battery (SFB) using a biomaterial-based piezo-ionic hydrogel from water hyacinth carboxymethyl cellulose, mitigating risks of high-power and toxic materials near human skin. The SFB's multi-layer active material enhances conductivity and reduces resistance, enabling a 1 cm^2 device to discharge for 10 + h below 0.4 V, with an areal capacity of 4.1 mAh cm^{-2} at 400 μA cm^{-2}. Furthermore, SFB with piezo-ionic hydrogel, when affixed to the elbow, generates a peak current of 115 nA cm^{-2} as the elbow is fully flexed. Consequently, SFB can be utilised for energy storage, along with force and bending sensing. This study opens new avenues in advancing research on ultra-low voltage batteries for wearable and biomedical devices.

1. Introduction

Fabricating ultra-low voltage energy-storage device is essential for advancing emerging technologies such as wearable technology, RF harvester, Internet of Things, remote sensing platforms, and medical devices [1]. Wearable healthcare devices equipped with flexible sweat-monitoring sensors also requires innovative, safe, and reliable energy-storage solutions to enable optimal functionality [2,3]. Sweat, an easily accessible biofluid, enables continuous monitoring of analytes, including inflammatory markers and cytokines, providing real-time insight into physiological conditions [3,4]. Secreted by eccrine glands, sweat contains abundant electrolytes and metabolites, making it a valuable source for both physiological sensing and powering wearable devices. Its electrolyte content (K^+, Ca^{2+}, Na^+, and Cl^-), has been widely utilised in batteries [5–7], sensors [8–10], supercapacitors [11–14], biofuel cells [15–17]. and few of them are summarised in Table ST1 in supporting information. The past decade has also seen rapid growth in E-textiles, where conductive fabrics interact with the environment to enable advanced smart-wearable technologies [18,19].

Hydrogels are three-dimensional polymeric networks synthesised through chemical and/or physical crosslinking, giving them excellent hydrophilicity and allowing them to absorb and retain large amounts of liquid while maintaining structural integrity [20]. A more advanced class of hydrogels—conductive hydrogels—has recently gained significant research interest due to their promising applications in flexible electronic devices. These materials combine a cross-linked polymer framework with electrical or ionic conductivity [21]. Piezo-ionic hydrogels exhibit ion-trapping and ion-releasing behaviour, in which ions are temporarily immobilised and subsequently mobilised in response to mechanical stress or strain. This enables the detection of pressure, force, and environmental changes, which can be transduced into capacitance, current, or resistance signals [22]. The unique mechanical and electrochemical properties of conductive hydrogels have enabled their use in energy-storage devices [23–27], sensors [28–33], bioelectronics [34–38], triboelectric nanogenerators [39–43], and epidermal patch electrodes [44–46].

This study presents a multifunctional ultra-low-voltage sweat-activated fabric battery (SFB) that incorporates a piezo-ionic hydrogel capable of generating electric charge in response to mechanical deformation, thereby opening new avenues in ultra-low-voltage battery research. To address concerns related to toxic electrolytes and high-power materials in close contact with skin, an eco-friendly biomaterial-based piezo-ionic hydrogel was developed using water-hyacinth-derived carboxymethyl cellulose (WHCMC) and α-chitin.

* Corresponding author.
E-mail addresses: mustehsan.beg@napier.ac.uk (M. Beg), L.Manjakkal@napier.ac.uk (L. Manjakkal).
[1] Equal authors

https://doi.org/10.1016/j.nanoen.2026.111729
Received 4 November 2025; Received in revised form 25 December 2025; Accepted 14 January 2026
Available online 15 January 2026
2211-2855/© 2026 The Authors. Published by Elsevier Ltd. This is an open access article under the CC BY-NC-ND license (http://creativecommons.org/licenses/by-nc-nd/4.0/).

Carboxymethyl cellulose is a water-soluble polymer known for its abundance, excellent film-forming ability, and mechanical robustness [47], α-Chitin possesses a highly crystalline, asymmetric structure, is derived from renewable resources, and exhibits hydrophilicity, biocompatibility, biodegradability, and customizable functional groups [48,49]. To fabricate the piezo-ionic hydrogel, cellulose was first extracted from water hyacinth and subsequently modified through a carboxymethylation reaction to produce WHCMC. The hydrogel was then synthesised by blending WHCMC and α-chitin in a 1:1 wt ratio with PEG-400, citric acid, and NaCl, followed by a freeze–thaw process, as illustrated in Fig. 1.

A multilayer anode and cathode were integrated into the conductive fabric, which acted as the current collector. The outermost layer of both electrodes consisted of an Ag/AgCl coating selected for its biocompatibility, stability, and efficient charge-transfer characteristics. The cathode's second layer comprised a Cu_2O/graphene composite, commonly used in biosensing applications due to its antibacterial properties, high surface area, and excellent electron-transfer capability. The anode's second layer contained Zn powder, chosen for its high electrochemical activity and stability in aqueous environments. The pairing of Cu_2O as an air-permeable cathode with Zn as a sweat-permeable anode, combined with the sweat electrolyte, yields an ultra-low-voltage device. Cu_2O possesses a relatively low redox potential, while Zn provides a stable, low-potential anode, resulting in a narrow operating voltage window. This constrained voltage range enhances safety, suppresses unwanted side reactions, and makes the system well suited for wearable and biomedical applications.

2. Results and Discussion

2.1. Piezo-ionic hydrogel characterisation

As shown in Fig. 2a, the image of the prepared 1 wt% WHCMC after water hyacinth nanofibers underwent surface modification through a carboxymethylation reaction. This modification improves the dispersion stability and water solubility of WHCMC, enhancing its suitability for composite-material applications. Details of the carboxymethylation reaction and the fabrication of the piezo-ionic hydrogel are provided in the Experimental Section. The Fourier-transform infrared (FTIR) spectrum of WHCMC (Fig. 2b) confirms successful synthesis. The absorption peak at 1600 cm^{-1} arises from the stretching vibration of the carboxyl group ($–COO^-$), while the peak at 1438 cm^{-1} corresponds to the carboxylate salt ($–COO^-$ Na^+). A broad band around 3400 cm^{-1} is attributed to the O–H stretching vibration.

The piezo-ionic hydrogel, shown in Fig. 2c, demonstrates its bendability, twistability, and foldability, highlighting its fundamental mechanical flexibility for use in batteries. The scanning electron microscopy (SEM) image in Fig. 2d reveals a nanofibrous morphology with a porous structure, primarily generated by the freeze–thaw process used during hydrogel fabrication. Three-dimensional reconstructions of the hydrogel (Fig. 2e) further illustrate this interconnected porous network. The wettability of the piezo-ionic hydrogel was assessed using contact-angle measurements (Fig. 2f). A 5 μL droplet of artificial sweat electrolyte placed on the surface was rapidly absorbed, disappearing within 0.3 s, indicating the hydrogel's high hydrophilicity and efficient fluid uptake.

TGA thermogram in Fig. 2g, illustrates that the piezo-ionic hydrogel exhibits a steady weight loss from room temperature to 150 ℃ primarily due to moisture evaporation and the loss of absorbed water from WHCMC and α-chitin. Between 150 ℃ and 250 ℃, PEG 400 evaporates, and citric acid decomposes, leading to a more significant weight loss. The major weight loss between 250 ℃ and 400 ℃ corresponds to the degradation and decomposition of WHCMC and α-chitin. In the final stage, NaCl, with its high decomposition temperature, remains as a stable residue, along with some potential carbonaceous residue. Fig. 2h shows representative stress–strain curves for the piezo-ionic hydrogel,

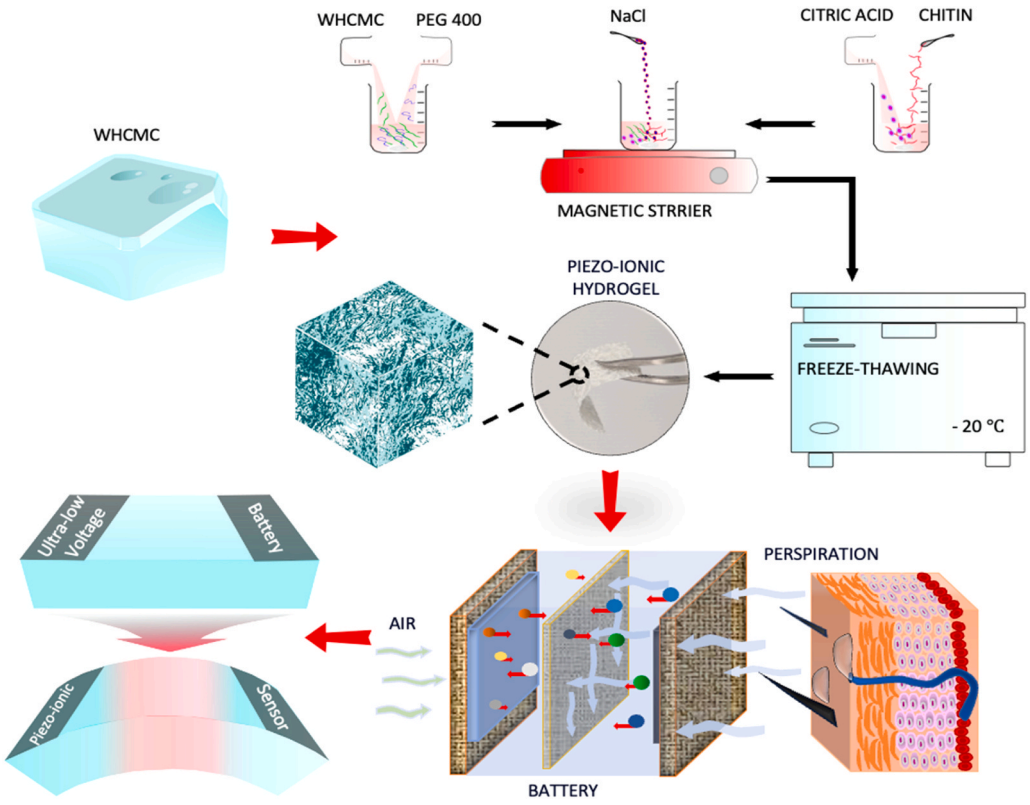

Fig. 1. Schematic illustration of SFB. The synthesis of the biomaterial-based piezo-ionic hydrogel, its integration into the air-and sweat-permeable battery, and its application as both an ultra-low voltage battery and a piezo-ionic sensor.

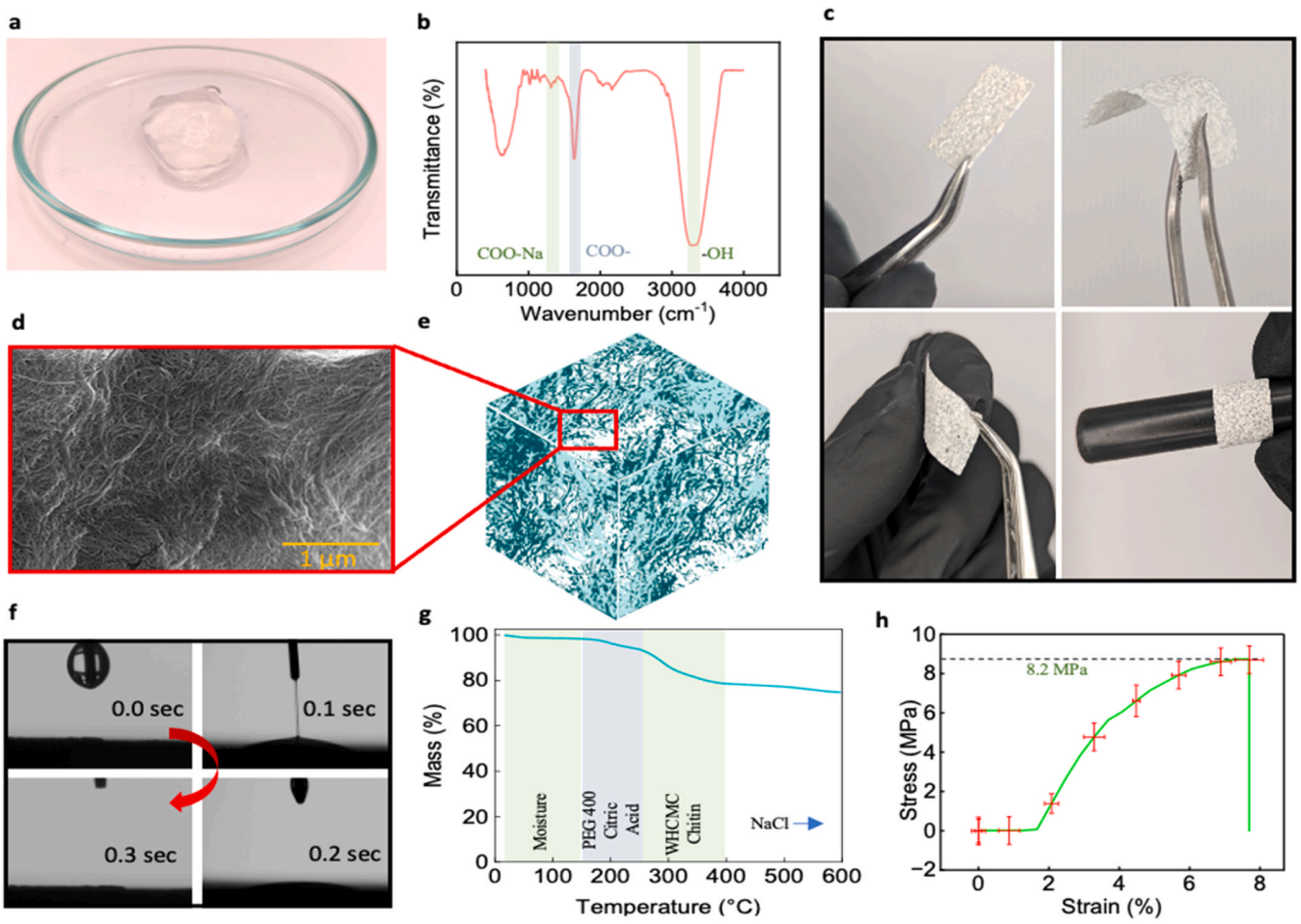

Fig. 2. Piezo-ionic hydrogel characterising. a, WHCMC after the carboxymethylation reaction. b, The FTIR of WHCMC. c, Piezo-ionic hydrogel's bendability, twistability, and foldability. d, Surface morphology of piezo-ionic hydrogel using SEM. e, 3D reconstructions of the piezo-ionic hydrogel. f, Contact angles of the artificial sweat electrolyte on piezo-ionic hydrogel. g, TGA thermogram. h, The tensile strength of piezo-ionic hydrogel.

which exhibits a tensile strength of 8.2 ∓ 0.687 MPa.

2.2. Multi-layer active material for SFB

The fabrication procedures for the three sweat-activated fabric batteries (SFB-1, SFB-2, and SFB-3) are illustrated in Fig. 3a–c. Detailed descriptions of SFB-1 and SFB-2 (Fig. 3a and Fig. 3b) are provided in the Supplementary Information (Figures S1 and S2), and additional fabrication steps are described in the Experimental Section. SFB-3 uses a conductive fabric as both the substrate and current collector, with an Ag/AgCl coating applied to both the cathode and anode. The multilayer SFB-3 incorporates a Cu_2O/graphene paste at the cathode and a dip-coated anode consisting of Zn powder, carbon black, and shellac binder.

Fig. 3d shows SEM images of the conductive fabric and the Ag/AgCl, Zn, and Cu_2O/graphene layers, (Zn, and Cu_2O/graphene) are common to all three devices (SFB-1, SFB-2, and SFB-3). The conductive fabric exhibits a woven morphology. The Ag/AgCl layer contains uniformly distributed spherical particles with an average diameter of ~2 μm, whereas the Zn layer consists of larger spherical particles (~4 μm) with a microporous, rough surface. In contrast, the Cu_2O/graphene coating displays a more uniform coverage with higher nano- and microporosity and a smoother surface. Additional SEM images and EDX spectra for the Ag/AgCl-coated fabric (Figure S3), Zn paste (Figure S4), and Cu_2O/graphene layer (Figure S5) are provided in the Supplementary Information.

In addition, Fig. 3e evaluates the wettability of each coated electrode surface through contact angle measurements using artificial sweat electrolyte. The results confirm the hydrophilic nature of all coatings, each exhibiting a lower contact angle than the original conductive fabric, which has a mean contact angle of 87.05° ∓ 0.1372. Lower contact angles indicate better wettability, which allows artificial sweat to spread more efficiently across the coating and enter surface pores. This enhances electrolyte absorption and shortens the ion-diffusion path, improving ion accessibility at the electrode/electrolyte interface [50]. Improved wettability also helps maintain continuous ionic contact during bending or deformation of the fabric, which is important for stable performance in wearable conditions. Furthermore, better wetting ensures faster re-hydration of the electrode after drying, allowing the SFB to recover its ionic conductivity more effectively [51]. Among the coatings, Zn paste demonstrates the most hydrophilicity, with a contact angle of 64.66° ∓ 0.4221. Its visible and larger microporous and rough surface, as seen in the SEM, might significantly enhance electrolyte wettability compared with Ag/AgCl and Cu_2O/graphene, which have mean contact angles of 78.65° ∓ 0.6323 and 84.37° ∓ 0.8326, respectively.

Alongside wettability, porosity of the electrodes plays an important part in air-and moisture-permeable electrodes. The porosity percentage of each coated electrode surface, determined from the SEM images, is shown in Fig. 3f. Zn and Cu_2O/graphene exhibit the highest surface porosity, with values of 13.65 % ∓ 0.0122 and 17.58 % ∓ 0.0372, respectively, compared to the conductive fabric and Ag/AgCl, which show porosity values of 1.57 % ∓ 0.0765 and 10.91 % ∓ 0.0384. The increased porosity of these coatings can be attributed to the composite nature of Zn and carbon black, and Cu_2O and graphene. Cu_2O/graphene,

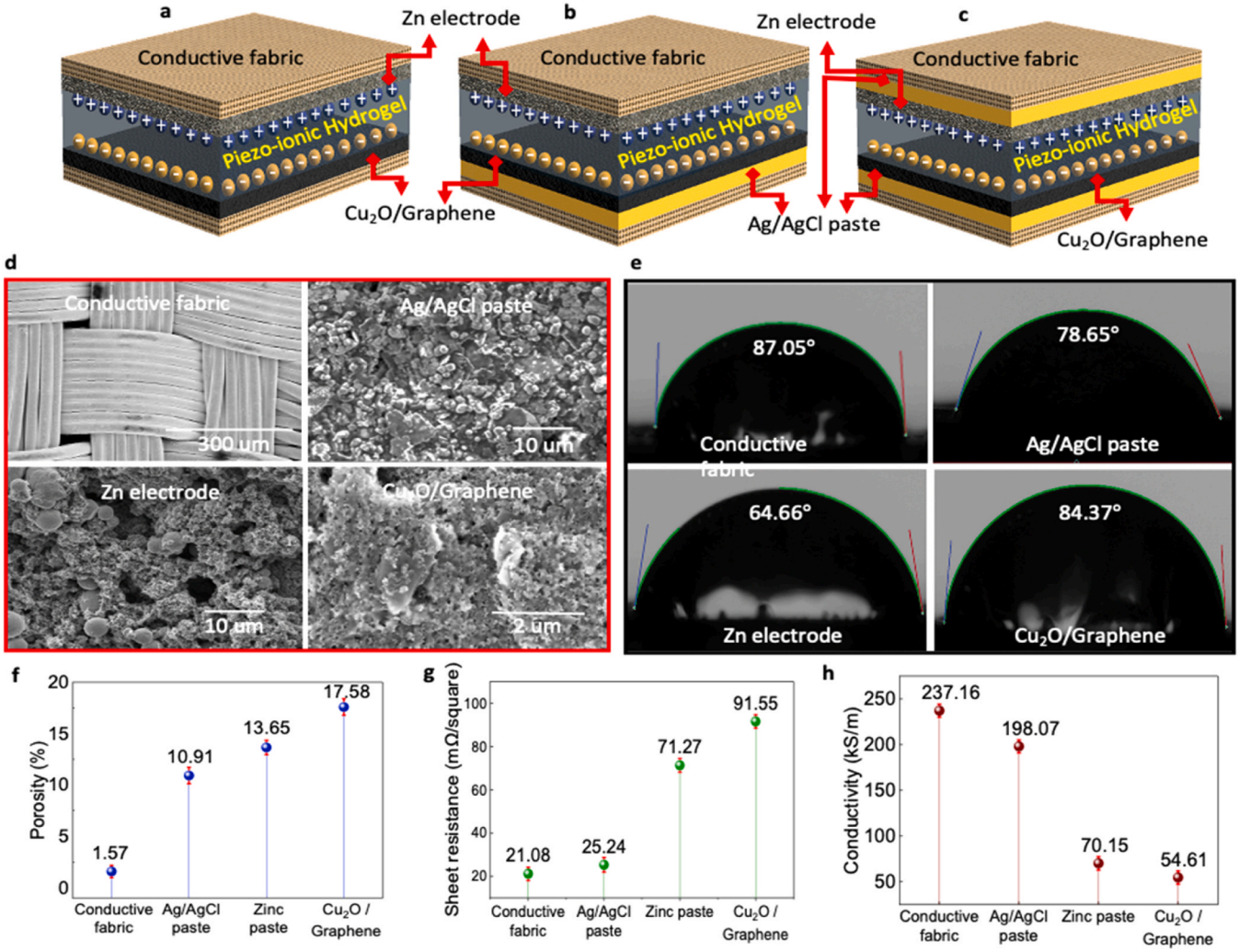

Fig. 3. SFBs designs and electrode characterisations. a-c. Three different SFBs designs and their components including the piezo-ionic hydrogel. d, SEM morphology of each layer in the multi-layer active material SFB. e, Wettability analysis of each layer, demonstrating the hydrophilic nature of the SFB. f, Surface porosity comparison of each layer in the SFB. g, Sheet resistance assessment of the SFB layers. h, Conductivity evaluation of the SFB layers.

resulting in a more porous and larger surface area of the electrode. Surface porosity further supports ionic transport by providing more open pathways for electrolyte penetration and increasing the effective electroactive area [52]. The highly porous Zn (13.65 %) and Cu_2O/graphene (17.58 %) layers therefore allow ions to reach a greater number of active sites, which facilitates more efficient charge transfer. In contrast, lower porosity, as observed in the Ag/AgCl coating, limits the accessible ion pathways. Higher porosity also reduces diffusion resistance because ions can move through interconnected pores rather than being restricted to surface-level transport. Additionally, porous structures retain electrolyte more effectively, helping maintain continuous ionic conduction during prolonged operation or mechanical movement [53]. Fig. 3g and Fig. 3h show the sheet resistance and conductivity of each coated electrode surface. The sheet resistance of conductive fabric and Ag/AgCl is 21.08 ∓ 0.0673 and 25.24 ∓ 0.0927 mΩ/square, while Zn and Cu_2O/graphene exhibit higher sheet resistances of 71.27 ∓ 0.0132 and 91.55 ∓ 0.0879 mΩ/square, respectively. The low sheet resistance of conductive fabric and Ag/AgCl can be attributed to the nylon-based conductive fabric, which is Ag-plated, and the high Ag content (60 %) in Ag/AgCl. As a result, the Ag-based conductive fabric and Ag/AgCl exhibit high conductivity values of 237.16 ∓ 0.0432 and 198.07 ∓ 0.0111 kS/m, respectively, compared to Zn's layer at 70.15 ∓ 0.1372 kS/m and Cu_2O/graphene's layer at 54.61 ∓ 0.0231 kS/m. The FTIR spectrum of the conductive fabric coated with Ag/AgCl and Zn paste is presented in Supplementary Information Figure S6. Additionally, Figure S7 displays the X-ray diffraction (XRD) patterns of both materials.

2.3. Multi-layer active material for SFB

Fig. 4a compares the cyclic voltammetry (CV) curve for the SFB devices at 20 $mV.s^{-1}$, showing that the coating of Ag/AgCl on both the positive and negative electrodes (SFB-3) exhibits the largest CV area, indicating higher capacity or more significant electrochemical reaction. Additionally, the reduction peak of below 2 mA cm^{-2} under ultra-low voltage of 0.5 V demonstrates high electrochemical efficiency and low resistance. The Nyquist plot (frequency range of 1 Hz to 1 MHz) intercept on the Z_{real} axis represents the solution resistance (R_s). During interaction with artificial sweat electrolytes and electrodes, the solution resistance in SFB-3 decreased further to 0.9 Ω, compared to 2.2 Ω for SFB-2 and 5.8 Ω for SFB-1, as indicated by their CV, as shown in Fig. 4b.

For the SFB-3, it was found that with the increasing scan rate, the redox peak current and CV area were increasing, indicating that the electrochemical reaction kinetics are improving with faster potential sweeps. This behaviour suggests enhanced charge transfer efficiency of multi-layer electrodes, as shown in Fig. 4c. The galvanostatic charge/discharge (GCD) curves shown in Fig. 4d at 400, 500, and 600 μA cm^{-2} show the discharge times of over 3.5, 8, 10 h, respectively, indicating

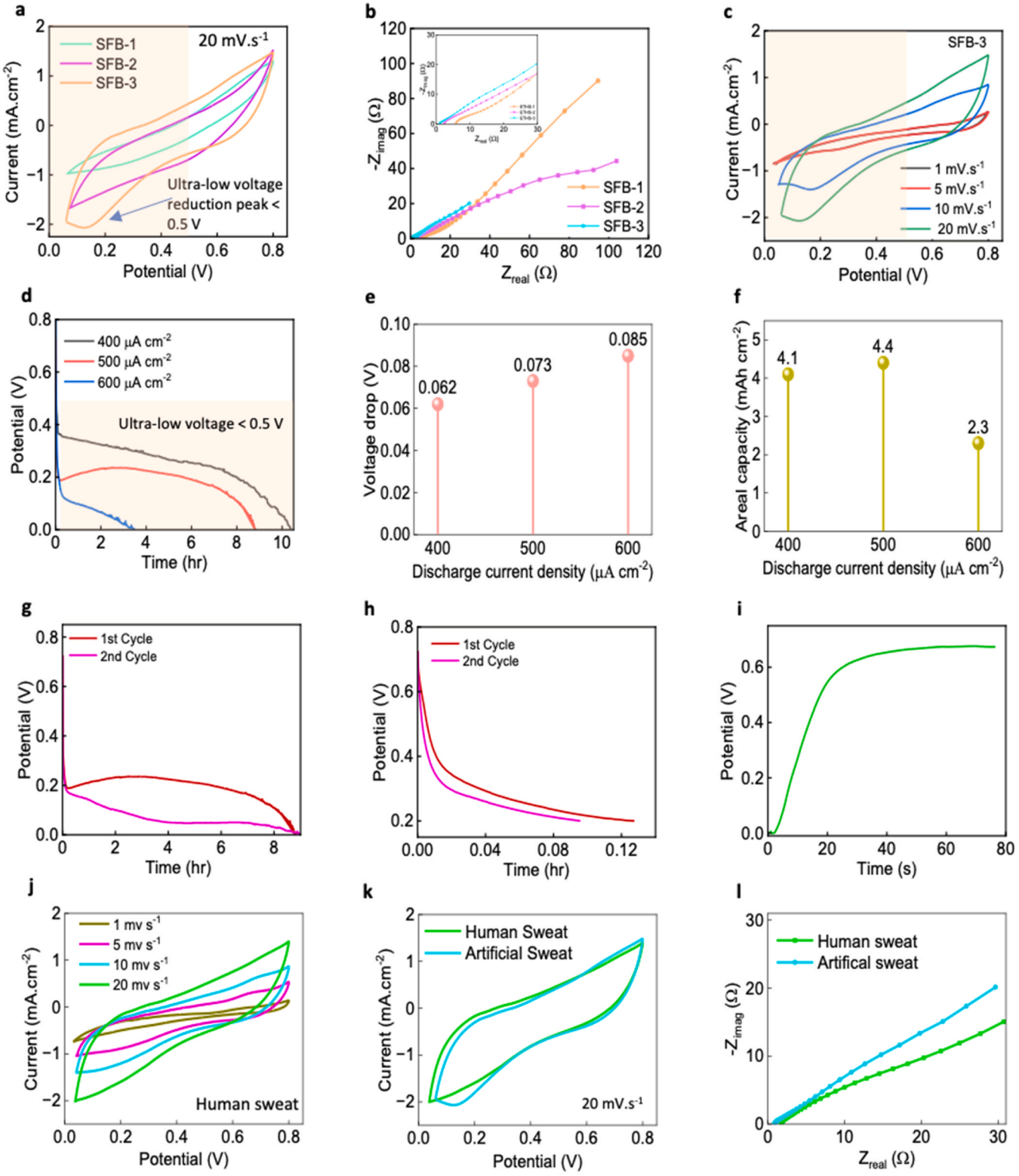

Fig. 4. Electrochemical characterisation of SFBs. a, Comparison of CV curve for of SFB-1, SFB-2 and SFB-3 at 20 mV s^{-1}. b, Comparison of the Nyquist plot from 1 MHz to 1 Hz for all three SFB with inset shows high frequency region. c, CV curve at 1, 5, 10, 20 mV s^{-1} for SFB-3. d, Discharge curve for SFB-3 at 400, 500, and 600 μA cm^{-2}. e, The voltage drop at each discharge current density. f, Discharge Areal capacities in mAh cm^{-2} for SFB-3. g, Cycle one and two of SFB-3 at 500 μA cm^{-2}. h, The discharge curve at the early stages of both cycles. i, the activation of SFB-3 occurs when a drop of artificial sweat is applied to the cathode side of the device. j, CV curve for of SFB-3 with human sweat at 1, 5, 10, 20 mV s^{-1}. k, Comparison of CV results between artificial and human sweat at 20 mV s^{-1}. l, Comparison of Nyquist plot results between artificial and human sweat from 1 MHz to 1 Hz.

high Areal capacity for SFB-3 at ultra-low voltage. Here, the extended discharge durations (3.5–10 + hours) observed in Fig. 4d are attributed to a combination of efficient ionic conduction through the hydrogel, favourable electrode kinetics, and limited moisture evaporation during testing. The WHCMCNF–chitin hydrogel used in the device forms a porous, hydrated polymer network that supports high ionic conductivity, comparable to some liquid electrolytes. These natural biopolymers exhibit strong hydrophilicity and hygroscopic behaviour, which help retain water and maintain ion transport pathways over prolonged durations. This is consistent with prior studies demonstrating hydrogel electrolytes retaining significant water and sustaining ionic conduction under ambient humidity conditions [54,55]. Additionally, the electrochemical interfaces—comprising Ag/AgCl, Cu_2O/graphene, and Zn–carbon paste—offer high surface area and stable redox activity, facilitating low-resistance charge transfer, especially under the ultra-low current conditions used in our tests. Similar performance has been reported for wearable batteries using matched redox couples and porous electrodes [56]. Finally, evaporation effects are mitigated by the hygroscopic nature of chitin and cellulose nanofibers, combined with testing under controlled ambient humidity. Hydrogels with similar biopolymer structures have retained electrochemical functionality, supporting our assertion that the long GCD times reflect genuine electrochemical behaviour rather than artifacts caused by dehydration [57]. These combined material and environmental factors validate the observed discharge performance as intrinsic to the device design. Fig. 4e, displays the voltage drop corresponding to each discharge current density, as the discharge current density increases, the voltage drop also increases due to greater polarization and higher resistive losses within the battery. The specific capacity measured from the discharge curve of the ETB-3 and observed values given in Fig. 4f showing at current density of 400 μA cm^{-2} the device areal capacity is 4.1 mAh cm^{-2}.

In Fig. 4g, the cycling performance of SFB-3 is shown, illustrating its behaviour as a single-use primary energy storage device. The discharge voltage decreases during the second cycle, and it fails to recharge during the third cycle. In Fig. 4h, comparison between the first and second cycles is presented, highlighting the discharge curve behaviour in the early stages of both cycles. Hence, the SFB operates as a primary, single-use sweat-activated Zn cell, with no capacity for recharge. This is evident from the cycling behaviour (Fig. 4g–h), where the device delivers a full discharge in the first cycle but cannot be restored thereafter, displaying a markedly reduced voltage in the second cycle and complete failure in the third. Such behaviour is characteristic of the irreversible Zn conversion reactions in aqueous systems, where Zn is oxidised to ZnO/$Zn(OH)_2$ and progressively undergoes corrosion and passivation, preventing any redeposition of metallic Zn, as discussed more broadly for Zn-based aqueous batteries [58]. The WHCMC/α-chitin hydrogel becomes electrochemically active only after sweat absorption (Fig. 4i), and subsequently begins to dehydrate during operation, leading to increased ionic resistance; this irreversible rise in resistance is consistent with behaviour reported for hydrogel electrolytes [59]. This trend is also reflected in the impedance measurements, where the solution resistance increases following activation with human sweat (Fig. 4l). The operational lifetime of over 10 h at 400 μA cm^{-2} (Fig. 4d–f) is determined by the available Zn and the volume of sweat absorbed into the hydrogel. Once the Zn is consumed and/or the hydrogel dries, the device cannot be reactivated beyond residual capacity, aligning with other reported sweat-activated Zn batteries designed for disposable wearable applications [7,56,60]. The SFB-3 exhibited a saturation voltage of 0.6 V as could be seen in Fig. 4i. In which a drop of artificial sweat electrolyte from pipette is dropped at the cathode side of SFB-3, initially the voltage stays around 0 V for initial 3 s before rising sharply to above 0.6 V as the electrolyte is absorbed through the fabric and on to the piezo-ionic hydrogel.

For human sweat electrolyte testing, sweat from the palm of the hand is used. As the human sweat is absorbed into the device, the CV curve shown in Fig. 4j is obtained at various scan rates. Fig. 4k, compares the results of artificial sweat and human sweat at 20 mV s^{-1}, showing similar behaviour. The slight difference observed can be attributed to the higher resistances in human sweat, as seen in Nyquist plot Fig. 4l, where the solution resistance of human sweat is 1.8 Ω, compared to 0.9 Ω for artificial sweat. Human sweat typically has lower and more variable ionic strength than standard artificial sweat formulations, which are prepared with fixed concentrations of NaCl, KCl, lactate, urea and other salts to mimic an average composition [61]. In real sweat, the total ion content, and the relative concentrations of Na^+, Cl^-, K^+, and other species vary substantially between individuals and with factors such as sweat rate, hydration status, acclimation, and collection site [62,63]. This lower and more heterogeneous ionic content generally leads to a lower bulk conductivity and therefore a higher measured impedance for human sweat compared with artificial sweat of fixed composition. In addition, human sweat contains proteins, lipids and other organics that are often absent or minimized in artificial formulations, and these components can contribute to interfacial effects or partial fouling, further increasing the apparent resistance [64].

Although many commercial wearable systems still operate at 1–1.8 V, there is a growing class of ultra-low-voltage electronics and microcontrollers specifically designed to function at or near 0.4 V to minimize power consumption. A representative example is the SleepWalker microcontroller which was designed for low-carbon wireless sensor nodes [65]. SleepWalker operates directly at 0.4 V in 65-nm CMOS and achieves only 7 μW/MHz at the full SoC level while still supporting 25-MHz operation. This demonstrates that 0.4 V power delivery can indeed drive practical, computationally capable ASICs without the need for intermediate boosting stages. In case where the circuits need higher voltage, standard boost converters can be used and the integration of multiple cells in series-parallel can achieve required voltage without compromising comfort and safety.

2.4. SFB with piezo-ionic hydrogel

Piezo-ionic devices are attractive because they generate electrical charges in response to mechanical stress, enabling both energy generation and force- or pressure-sensing applications. Figs. 5a and 5b present schematic illustrations of the mechanical stress and bending applied to SFB-3. The piezo-ionic hydrogel, composed of α-chitin fibres and WHCMC, contains inherent moisture retained through hydrophilic functional groups (–OH, $–COO^-$, $–NHCOCH_3$), which promote water retention and ion diffusion. When mechanical stress is applied, a localized potential difference is produced, driving the migration of Na^+ and Cl^- ions within the hydrogel, as illustrated in Fig. 5c.

In Fig. 5d, when force is applied to the 1 cm^2 SFB-3, current peaks are observed, corresponding to the application of varying forces, while in Fig. 5e shows negative current peaks are observed when varying forces are applied, indicating a response to mechanical stimuli when the polarity of SFB-3 is reversed. In Fig. 5f, SFB-3 is bent in 20°, 40°, and 60°, resulting in peak currents of 36, 44, and 68 nA $cm^{-2,}$ while in Fig. 5g, reverse bending of SFB-3 also showed positive currents. However, the reverse bending exhibits a lower current, approximately half the value of the forward bending current, likely due to asymmetrical ion transport dynamics, variations in the internal strain distribution, and differences in electrode contact resistance. Figs. 5h and 5i, show the force applied and the bending of SFB-3 for approximately one minute, along with the resulting current. The dynamic piezo-ionic effect shows initial instantaneous current peak from Na^+ and Cl^- ions movement within a material in response to mechanical deformation, while the capacitive piezo-ionic region, involves Na^+ and Cl^- ion accumulation at interfaces or within the material, behaving similarly to a capacitor. When the SFB-3 is affixed to the wrist, elbow, and neck, its resulting peak currents when half and fully bent are shown in Fig. 5j, Fig. 5k, and Fig. 5l. The highest peak current was observed when SFB-3 was affixed to the elbow, generating a peak current of 115 nA cm^{-2} when the elbow was fully flexed. The

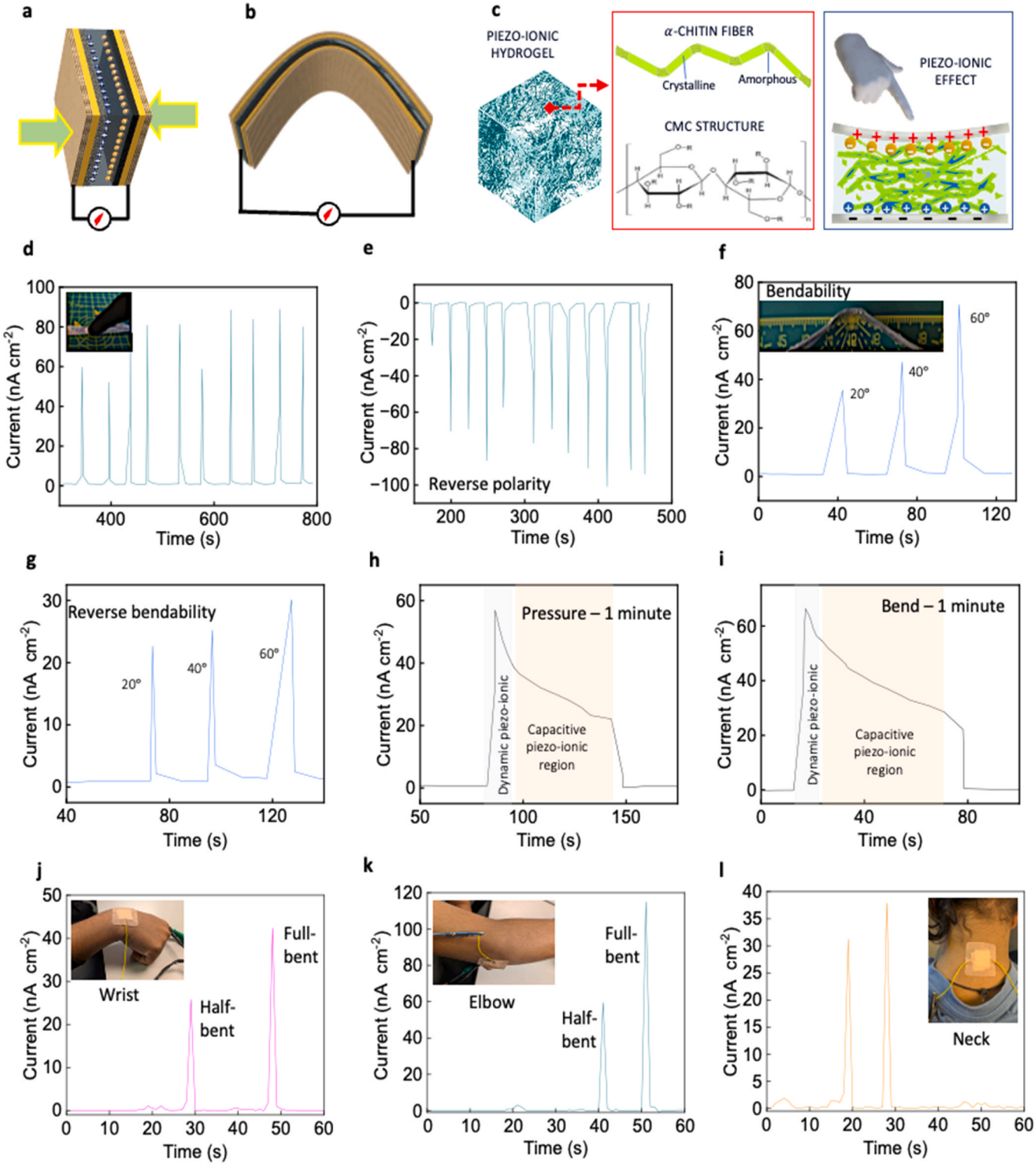

Fig. 5. Piezo-ionic sensor characterisation. a-b, Schematic diagram of force and bending stress applied to SFB-3 to produce electrical charge. c, Piezo-ionic mechanism. d, Various forces were applied to SFB-3, and its resulting current peaks. e, Various force applied to SFB-3 in reserved polarity. f-g, SFB-3 bend in both directions by 20°, 40°, and 60°. h-i, Force and bending of SFB-3 for approximately one minute. j-l, The SFB-3 is affixed to the wrist, elbow, and neck and its peak current results.

asymmetric current output can be explained by differences in the strain-induced ionic flux during forward and reverse bending. When the device is bent forward, the hydrogel experiences a larger strain gradient ($\varepsilon = y/R$), which generates a stronger internal electric field and produces higher ionic drift velocity $v = \mu E$. This results in a greater net ionic flux $J = -D\nabla c + \mu cE$, enhancing the piezo-ionic current [66,67]. In contrast, reverse bending places the active ionic region closer to the neutral axis, reducing both the effective strain and the resulting concentration gradient, and therefore leading to a noticeably lower current. This behaviour is consistent with previously reported ion-mobility-dominated piezo-ionic systems [66,67].

To emphasise the multifunctional nature of the system, it is

important to note that both the sweat-activated electrochemical discharge and the piezo-ionic current generation originate from the same SFB-3 device architecture and rely on ion transport within the shared WHCMC/α-chitin hydrogel layer. The piezo-ionic experiments presented in Fig. 5d–l were carried out using the same device examined electrochemically in Fig. 4, demonstrating that the sensing behaviour does not arise from a separate structure but from an additional functional response of the integrated platform. Furthermore, the on-body bending tests (Fig. 5j–l) show that the device maintains stable ionic activity under mechanical deformation, confirming that SFB-3 can support both energy-storage and sensing functions within a single system. This unified operational behaviour highlights SFB-3 as a multifunctional device rather than two independent concepts.

While our study demonstrates the functionality of the SFB using a real human sweat sample, we recognize the limitation of relying on a single donor. Human sweat is a highly heterogeneous biofluid, with variations in pH (4.5–7.0), salinity (e.g., NaCl ranging from 20 to 60 mM), and metabolite levels (such as lactate, urea, glucose) depending on individual physiology, diet, hydration, and anatomical collection site [68]. This inter-subject variability can influence ionic conductivity and electrochemical reaction rates, potentially impacting device voltage, discharge time, and sensor response. However, our system was engineered with robust materials — such as Zn/carbon and Cu_2O/graphene electrodes — that have been validated in wearable power sources for stable performance across wide physiological conditions [56]. In one of the recent work, further reinforces the importance of accounting for sweat composition variability in the design of wearable bioelectronics [69]. Additionally, our ionic hydrogel matrix, rich in hygroscopic biopolymers, is inherently capable of buffering moderate ionic fluctuations, potentially stabilizing performance across varying sweat chemistries. While artificial sweat testing across multiple compositions was not conducted in this study, we plan to include such tests, along with a diverse cohort of human donors, in future work to rigorously evaluate device robustness in real-world conditions.

3. Conclusions

In summary, in the pursuit of fabricating a multifunctional ultra-low voltage battery for future ultra-low power applications, water hyacinth cellulose nanofibers were surface modified through a carboxymethylation reaction to produce water-soluble WHCMC. The piezo-ionic hydrogel was then synthesised using WHCMC, α-chitin, PEG 400, citric acid, and NaCl via the freeze-thawing method. The piezo-ionic hydrogel is utilized in three different types of SFB with artificial sweat electrolyte, where SFB-3 demonstrated the best performance. It consists of a conductive fabric as a current collector, with a multi-layer active material comprising Ag/AgCl and Cu_2O/graphene coated on top of the conductive fabric as the positive electrode. For the negative electrode, a uniform ink containing Zn powder, carbon black, and shellac is prepared and coated onto the conductive fabric along with Ag/AgCl, forming the battery's negative electrode. The results showed a significant increase in discharge areal capacity reaching 4.1 mAh cm^{-2} at 400 μA cm^{-2} discharging below 0.4 V, with the lowest solution resistance of 0.9 Ω. The CV and EIS measurements using human sweat electrolyte exhibited similar performance to those with artificial sweat electrolyte.

Additionally, the multifunctional SFB-3, incorporating a piezo-ionic hydrogel, demonstrated great potential as a piezo-ionic sensor. This was particularly evident in bendability tests, where different bending angles produced distinct peak currents: 36 nA cm^{-2} at 20°, 44 nA cm^{-2} at 40°, and 68 nA cm^{-2} at 60°. Furthermore, when SFB-3 was affixed to the wrist, elbow, and neck, the highest peak current of 115 nA cm^{-2} was observed. These results highlight the versatility of the multifunctional SFB-3, showcasing its potential not only as a sustainable energy storage device but also as a piezo-ionic sensor for wearable and biomedical applications.

4. Experimental section

4.1. Materials and methods

Water hyacinth (WH) cellulose pulp (1 wt%), Isopropyl alcohol (IPA), ethanol, methanol, monochloroacetic acid (MCA), acetic acid, NaOH, NaHCO3 and DI water. Chitin, polyethene glycol (PEG 400), citric acid, NaCl. Electrically conductive fabric (Conductive Fabric, Ripstop, Kitronik), Ag/AgCl paste, Cu2O/graphene paste (JE Solution), Zn powder, carbon paste, shellac, Ag conductive ink (RS Components 186–3600), insulating paste (TPU Protective Ink, JE Solution).

4.2. Preparation of WHCMC

Cellulose is derived from water hyacinth was extracted using a technique outlined by Sun, D. *et al.* [70]. The cellulose nanofibers were surface modified by carboxymethylation reaction using the procedure adapted from Wågberg, L. et al. [71]. 15 g of WH cellulose pulp was solvent exchanged twice to ethanol. 1.4 g of MCA (monochloroacetic acid) was dissolved in 70 ml IPA and mixed with the ethanol-exchanged cellulose pulp. The mixture was allowed to soak for 30 min with mixing. A solution of 2.25 g of NaOH and 70 ml methanol was added to 280 ml of IPA that has been heated to 65 ℃ in an oil jacketed reaction cylinder. The cellulose-MCA-IPA mixture was added to the mixture in the reaction cylinder and allowed to react for 1 h. After 1 h, the suspension was filtered and washed 3 times with water (DI), once with 0.1 M acetic acid and 4 times with water. To convert the carboxymethyl groups to the more swelling sodium form, the surface modified pulp was dispersed in 280 ml of 4 wt% $NaHCO_3$ for 1 h (converts to sodium) before being washed 5 times with water. The cellulose pulp was diluted to 1 wt% and subjected to 2 passes through a high-pressure homogenisation using a PSI-20 homogeniser (Adaptive Instruments, UK) at 200 MPa resulting in synthesis of WHCMC.

4.3. Preparation of eco-friendly WHCMC/ α-chitin hydrogel

The water-soluble polysaccharides, WHCMC and ***α***-chitin with PEG 400, citric acid, NaCl at a weight ratio of 1: 1: 0.25: 0.25: 1 is added to the beaker, with 50 ml of DI water. The resulting solution is mixed using a T25 digital ULTRA TURRAX for 4 min at 7500 rpm, followed by 1 min at 10000 rpm, and then transferred it to a glass petri dish with a diameter of 15 cm. To induce crosslinking, the resulting mixture undergoes a freeze-thaw cycle at −20 ℃ and 25 ℃ before being subjected to 30 ℃ in an air oven for 24 h and it resulting in a ~150 ***μ***m piezo-ionic hydrogel.

4.4. Fabrication of SFBs

Electrically conductive cloth is used as a substrate for the fabrication of SFB, utilising Ag/AgCl paste applied with the doctor blade technique on top of the subtract and heat treated at 80 ℃ for 1 hrs. Cu2O/graphene paste is used as the active material for the positive electrode of SFB and also heat treated at 80 ℃ for 1 hrs with the active area of 1 cm^2, the negative battery electrode is also comprised of Ag/AgCl paste coated on top of the substrate, with Zn powder /carbon black / shellac uniform ink is prepared by magnetic stirring for 20 min at room temperature (25 ℃), at the weight ratio of 9: 0.25: 0.75, dip-coated on top for 30 s and dried 80 ℃ for 1 hrs. WHCMC/ ***α***-chitin Hydrogel is used in-between the positive and negative electrodes with artificial sweat as an electrolyte. For both electrodes, a copper wire in connected using Ag conductive ink, and then dried for 20 min in the oven at 60 ℃ Following this, an insulating layer is applied over the Ag conductive ink and dried for 30 min in an air oven at 80°C. For SFB-1 and SFB-2, same steps are taken as previously explained, expect that SFB-1 has no Ag/AgCl layers and SFB-2 has Ag/AgCl only at the positive electrode.

4.5. Preparation of artificial sweat

Artificial sweat was prepared by using the reported method [72,73] which consist of, 0.5 %wt of NaCl (Sodium Chloride), 0.1 %wt of KCl (Potassium Chloride), 0.1 %wt of lactic acid, and 0.1 % of Urea [all chemicals purchased from sigma- Aldrich] were added to 50 ml of DI (Deionized water) water and mixed using a magnetic stirrer for 20 min. Then the pH of the solution was maintained at 6.3 by adding 0.1 M NaOH (Sodium Hydroxide) (prepared by dissolving 0.2 g of NaOH in 50 ml of DI water) and 0.1 M lactic acid (prepared by dissolving 0.45 ml of lactic acid in 50 ml of DI water). To maintain pH a digital pH meter was used after calibrating the meter with a 7.01 pH calibration solution.

4.6. Characterisation

The TMG universal benchtop material thickness gauge, compliant with ASTM/DIN/EN/ISO standards, is employed to assess the thickness of the WHCMC/α-chitin Hydrogel. The surface structure of the pristine WHCMC/α-chitin Hydrogel are examined utilising a Scanning Electron Microscope (SEM, S4800, Hitachi Company) with an acceleration voltage set at 3 kV. The contact angles of the WHCMC/α-chitin Hydrogel with artificial sweat is determined with 5 μL droplet area, utilising a contact angle goniometer equipped with image capture (Ossila contact angle Goniometer L2004A1). The TGA testing of the piezo-ionic hydrogel is done on TA TGA 5500, from room temp to 600 ° at 10 °C/min. The Electrochemical characterisations, including cyclic voltammetry (CV), electrochemical impedance spectroscopy (EIS), and the evaluation of SFBs performance (GCD), were conducted using an Ametek Modulab electrochemical system. Cyclic voltammetry for the SFB was performed over scan rates ranging from 1 mV s^{-1}–20 mV s^{-1}, with a potential range of 0–0.8 V. Electrochemical impedance spectroscopy was conducted over a frequency range of 1 MHz to 1 Hz. Galvanostatic charge-discharge (GCD) measurements were executed at various current densities, within a potential range of 0–0.8 V. The sheet resistance and electrical conductivity was measured using Osscila Four-Point Probe.

CRediT authorship contribution statement

Keng Goh: Writing – original draft, Methodology, Investigation. **Hongnian Yu:** Writing – original draft, Visualization, Supervision, Methodology, Investigation. **Libu Manjakkal:** Writing – review & editing, Writing – original draft, Supervision, Resources, Project administration, Methodology, Investigation, Funding acquisition, Formal analysis, Data curation, Conceptualization. **Mustehsan Beg:** Writing – original draft, Validation, Methodology, Investigation, Formal analysis, Data curation, Conceptualization. **Prasutha Rani Markapudi:** Writing – original draft, Validation, Methodology, Investigation. **Keith M. Alcock:** Writing – original draft, Methodology, Investigation. **Vishnu Sam:** Writing – original draft, Visualization, Methodology, Investigation, Formal analysis, Data curation. **Jithin Kanathedath:** Writing – original draft, Visualization, Methodology, Investigation.

Ethical approval

The human sweat used for testing was provided by the co-author as a volunteer, and the author provided written consent. No ethical approval was required in this case.

Declaration of Competing Interest

The authors declare that they have no known competing financial interests or personal relationships that could have appeared to influence the work reported in this paper.

Acknowledgements

This work was supported by the Carnegie Trust for the Universities of Scotland Grant (R2552–00) and Edinburgh Napier University SCEBE starter Grant (N480–001).

Appendix A. Supporting information

Supplementary data associated with this article can be found in the online version at doi:10.1016/j.nanoen.2026.111729.

Data Availability

Data will be made available on request.

References

[1] L. Portilla, J. Zhao, Y. Wang, L. Sun, F. Li, M. Robin, M. Wei, Z. Cui, L.G. Occhipinti, T.D. Anthopoulos, V. Pecunia, Ambipolar deep-subthreshold printed-carbon-nanotube transistors for ultralow-voltage and ultralow-power electronics, ACS Nano 14 (10) (2020) 14036–14046.
[2] N. Davis, J. Heikenfeld, C. Milla, A. Javey, The challenges and promise of sweat sensing, Nat. Biotechnol. (2024) 1–12.
[3] R.P. Hirten, K.-C. Lin, J. Whang, S. Shahub, D. Helmus, S. Muthukumar, B.E. Sands, S. Prasad, Longitudinal assessment of sweat-based TNF-alpha in inflammatory bowel disease using a wearable device, Sci. Rep. 14 (1) (2024).
[4] M. Chung, G. Fortunato, N. Radacsi, Wearable flexible sweat sensors for healthcare monitoring: a review, J. R. Soc. Interface 16 (159) (2019) 20190217.
[5] X. Huang, Y. Liu, J. Zhou, S.K. Nejad, T.H. Wong, Y. Huang, H. Li, C.K. Yiu, W. Park, J. Li, J. Su, L. Zhao, K. Yao, M. Wu, Z. Gao, D. Li, J. Li, R. Shi, X. Yu, Garment embedded sweat-activated batteries in wearable electronics for continuous sweat monitoring, npj Flex. Electron. 6 (1) (2022).
[6] Y. Liu, X. Huang, J. Zhou, C.K. Yiu, Z. Song, W. Huang, S.K. Nejad, H. Li, T. H. Wong, K. Yao, L. Zhao, W. Yoo, W. Park, J. Li, Y. Huang, H.R. Lam, E. Song, X. Guo, Y. Wang, Z. Dai, L. Chang, W.J. Li, Z. Xie, X. Yu, Stretchable sweat-activated battery in skin-integrated electronics for continuous wireless sweat monitoring, Adv. Sci. 9 (9) (2022) 2104635.
[7] A. Bandodkar, S. Lee, I. Huang, W. Li, S. Wang, C.-J. Su, W. Jeang, T. Hang, S. Mehta, N. Nyberg, Sweat-activated biocompatible batteries for epidermal electronic and microfluidic systems, Nat. Electron. 3 (9) (2020) 554–562.
[8] C.F. Greyling, A. Ganguly, A.U. Sardesai, N.K.M. Churcher, K.C. Lin, S. Muthukumar, S. Prasad, Passive sweat wearable: a new paradigm in the wearable landscape toward enabling “detect to treat” opportunities, Wiley Interdiscip. Rev. Nanomed. Nanobiotechnol. 16 (1) (2024) e1912.
[9] D. Jiang, Y. Zhu, Z. Sun, Z. Zhu, Q. He, X. Huang, Y. Yang, Y. Ge, Q. Zhang, Y. Wang, A silver nanowires@ Prussian blue composite aerogel-based wearable sensor for noninvasive and dynamic monitoring of sweat uric acid, Chem. Eng. J. (2024) 150220.
[10] X. Liu, T. Li, T.-C. Lee, Y. Sun, Y. Liu, L. Shang, Y. Han, W. Deng, Z. Yuan, A. Dang, Wearable plasmonic sensors engineered via active-site maximization of TiVC MXene for universal physiological monitoring at the molecular level, ACS Sens. 9 (1) (2024) 483–493.
[11] J.T. Henriques, C.C. Do Carmo, A. Marques, I.M.M. Ferreira, A.C. Baptista, Carbon threads supercapacitors for washable e-textile applications: configurations and electrochemical performance, ACS Appl. Eng. Mater. 2 (2) (2024) 415–421.
[12] S. Selvam, S. Praveenkumar, J.-H. Yim, Cyclodextrin incorporated textile supercapacitor/piezo-triboelectric nanogenerator hybrid system for versatile temperature dependent wearable wireless devices, Chem. Eng. J. 482 (2024) 148929.
[13] H. Hong, H. Tu, L. Jiang, Y. Du, C.-p Wong, Advances in fabric-based supercapacitors and batteries: Harnessing textiles for next-generation energy storage, J. Energy Storage 75 (2024) 109561.
[14] M. Beg, K.M. Alcock, A. Titus Mavelil, D. O’Rourke, D. Sun, K. Goh, L. Manjakkal, H. Yu, Paper supercapacitor developed using a manganese dioxide/carbon black composite and a water hyacinth cellulose nanofiber-based bilayer separator, ACS Appl. Mater. Interfaces 15 (44) (2023) 51100–51109.
[15] S. Guan, Y. Yang, Y. Wang, X. Zhu, D. Ye, R. Chen, Q. Liao, A dual-functional MXene-based bioanode for wearable self-charging biosupercapacitors, Adv. Mater. 36 (1) (2024) 2305854.
[16] I. Shitanda, N. Loew, S. Tsujimura, Printable Wearable Self-Powered Biosensing System Based on Paper-Based Biofuel Cells Using Porous Carbon Material. Wearable Biosensing in Medicine and Healthcare, Springer, 2024, pp. 379–397.
[17] Y. Yuan, Z. Zhang, J. Cao, X. Zhao, L. Ye, G. Wang, Self-adhesive wearable poly (vinyl alcohol)-based hybrid biofuel cell powered by human bio-fluids, Biosens. Bioelectron. 247 (2024) 115930.
[18] M. Krifa, Electrically conductive textile materials—application in flexible sensors and antennas, Textiles 1 (2) (2021) 239–257.
[19] H.L.O. Júnior, R.M. Neves, F.M. Monticeli, L. Dall Agnol, Smart fabric textiles: recent advances and challenges, Textiles 2 (4) (2022) 582–605.
[20] H. Baniasadi, R. Abidnejad, M. Fazeli, J. Lipponen, J. Niskanen, E. Kontturi, J. Seppälä, O.J. Rojas, Innovations in hydrogel-based manufacturing: a

comprehensive review of direct ink writing technique for biomedical applications, Adv. Colloid Interface Sci. (2024) 103095.
[21] Y. Wu, E. Chen, X. Weng, Z. He, G. Chang, X. Pan, J. Liu, K. Huang, K. Huang, M. Lei, Conductive polyvinyl alcohol/silver nanoparticles hydrogel sensor with large draw ratio, high sensitivity and high stability for human behavior monitoring, Eng. Sci. 18 (2022) 113–120.
[22] J. Chen, F. Liu, T. Abdiryim, X. Liu, An overview of conductive composite hydrogels for flexible electronic devices, Adv. Compos. Hybrid. Mater. 7 (2) (2024) 1–37.
[23] S. Huang, L. Hou, T. Li, Y. Jiao, P. Wu, Antifreezing hydrogel electrolyte with ternary hydrogen bonding for high-performance zinc-ion batteries, Adv. Mater. 34 (14) (2022) 2110140.
[24] W. Sun, Z. Xu, C. Qiao, B. Lv, L. Gai, X. Ji, H. Jiang, L. Liu, Antifreezing proton zwitterionic hydrogel electrolyte via ionic hopping and grotthuss transport mechanism toward solid supercapacitor working at− 50° C, Adv. Sci. 9 (27) (2022) 2201679.
[25] S. Wu, D. Lou, H. Wang, D. Jiang, X. Fang, J. Meng, X. Sun, J. Li, One-pot synthesis of anti-freezing carrageenan/polyacrylamide double-network hydrogel electrolyte for low-temperature flexible supercapacitors, Chem. Eng. J. 435 (2022) 135057.
[26] J. Yang, X. Hu, X. Fang, L. Fan, G. Qin, Z. Zhang, J. Xu, Y. Liang, Q. Chen, Tough and redox-mediated alkaline gel polymer electrolyte membrane for flexible supercapacitor with high energy density and low temperature resistance, J. Membr. Sci. 650 (2022) 120386.
[27] X. Zhu, C. Ji, Q. Meng, H. Mi, Q. Yang, Z. Li, N. Yang, J. Qiu, Freeze-tolerant hydrogel electrolyte with high strength for stable operation of flexible zinc-ion hybrid supercapacitors, Small 18 (16) (2022) 2200055.
[28] J. Wen, J. Tang, H. Ning, N. Hu, Y. Zhu, Y. Gong, C. Xu, Q. Zhao, X. Jiang, X. Hu, Multifunctional ionic skin with sensing, UV-filtering, water-retaining, and anti-freezing capabilities, Adv. Funct. Mater. 31 (21) (2021) 2011176.
[29] Y. Feng, H. Liu, W. Zhu, L. Guan, X. Yang, A.V. Zvyagin, Y. Zhao, C. Shen, B. Yang, Q. Lin, Muscle-inspired MXene conductive hydrogels with anisotropy and low-temperature tolerance for wearable flexible sensors and arrays, Adv. Funct. Mater. 31 (46) (2021) 2105264.
[30] Y. Jiao, Y. Lu, K. Lu, Y. Yue, X. Xu, H. Xiao, J. Li, J. Han, Highly stretchable and self-healing cellulose nanofiber-mediated conductive hydrogel towards strain sensing application, J. Colloid Interface Sci. 597 (2021) 171–181.
[31] X. Yu, W. Qin, X. Li, Y. Wang, C. Gu, J. Chen, S. Yin, Highly sensitive, weatherability strain and temperature sensors based on AgNPs@ CNT composite polyvinyl hydrogel, J. Mater. Chem. A 10 (28) (2022) 15000–15011.
[32] T.H. Park, S. Park, S. Yu, S. Park, J. Lee, S. Kim, Y. Jung, H. Yi, Highly sensitive on-skin temperature sensors based on biocompatible hydrogels with thermoresponsive transparency and resistivity, Adv. Healthc. Mater. 10 (14) (2021) 2100469.
[33] W. Liu, R. Xie, J. Zhu, J. Wu, J. Hui, X. Zheng, F. Huo, D. Fan, A temperature responsive adhesive hydrogel for fabrication of flexible electronic sensors, npj Flex. Electron. 6 (1) (2022) 68.
[34] D. Gan, T. Shuai, X. Wang, Z. Huang, F. Ren, L. Fang, K. Wang, C. Xie, X. Lu, Mussel-inspired redox-active and hydrophilic conductive polymer nanoparticles for adhesive hydrogel bioelectronics, NanoMicro Lett. 12 (2020) 1–16.
[35] M. Yang, X. Ren, T. Yang, C. Xu, Y. Ye, Z. Sun, L. Kong, B. Wang, Z. Luo, Polypyrrole/sulfonated multi-walled carbon nanotubes conductive hydrogel for electrochemical sensing of living cells, Chem. Eng. J. 418 (2021) 129483.
[36] X. Ren, M. Yang, T. Yang, C. Xu, Y. Ye, X. Wu, X. Zheng, B. Wang, Y. Wan, Z. Luo, Highly conductive PPy–PEDOT: PSS hybrid hydrogel with superior biocompatibility for bioelectronics application, ACS Appl. Mater. Interfaces 13 (21) (2021) 25374–25382.
[37] Y. Jiang, X. Zhang, W. Zhang, M. Wang, L. Yan, K. Wang, L. Han, X. Lu, Infant skin friendly adhesive hydrogel patch activated at body temperature for bioelectronics securing and diabetic wound healing, ACS Nano 16 (6) (2022) 8662–8676.
[38] I.K. Han, K.I. Song, S.M. Jung, Y. Jo, J. Kwon, T. Chung, S. Yoo, J. Jang, Y.T. Kim, D.S. Hwang, Electroconductive, adhesive, non-swelling, and viscoelastic hydrogels for bioelectronics, Adv. Mater. 35 (4) (2023) 2203431.
[39] M. Wu, X. Wang, Y. Xia, Y. Zhu, S. Zhu, C. Jia, W. Guo, Q. Li, Z. Yan, Stretchable freezing-tolerant triboelectric nanogenerator and strain sensor based on transparent, long-term stable, and highly conductive gelatin-based organohydrogel, Nano Energy 95 (2022) 106967.
[40] Y. Liu, T.H. Wong, X. Huang, C.K. Yiu, Y. Gao, L. Zhao, J. Zhou, W. Park, Z. Zhao, K. Yao, Skin-integrated, stretchable, transparent triboelectric nanogenerators based on ion-conducting hydrogel for energy harvesting and tactile sensing, Nano Energy 99 (2022) 107442.
[41] Y. Feng, J. Yu, D. Sun, C. Dang, W. Ren, C. Shao, R. Sun, Extreme environment-adaptable and fast self-healable eutectogel triboelectric nanogenerator for energy harvesting and self-powered sensing, Nano Energy 98 (2022) 107284.
[42] H. Sun, Y. Zhao, C. Wang, K. Zhou, C. Yan, G. Zheng, J. Huang, K. Dai, C. Liu, C. Shen, Ultra-Stretchable, durable and conductive hydrogel with hybrid double network as high performance strain sensor and stretchable triboelectric nanogenerator, Nano Energy 76 (2020) 105035.
[43] W. Gao, Z. Lei, C. Zhang, X. Liu, Y. Chen, Stretchable and freeze-tolerant organohydrogel thermocells with enhanced thermoelectric performance continually working at subzero temperatures, Adv. Funct. Mater. 31 (43) (2021) 2104071.
[44] Z. Yu, P. Wu, Water-resistant ionogel electrode with tailorable mechanical properties for aquatic ambulatory physiological signal monitoring, Adv. Funct. Mater. 31 (51) (2021) 2107226.
[45] Y. Liu, C. Wang, J. Xue, G. Huang, S. Zheng, K. Zhao, J. Huang, Y. Wang, Y. Zhang, T. Yin, Body temperature enhanced adhesive, antibacterial, and recyclable ionic hydrogel for epidermal electrophysiological monitoring, Adv. Healthc. Mater. 11 (15) (2022) 2200653.
[46] X. Zhou, A. Rajeev, A. Subramanian, Y. Li, N. Rossetti, G. Natale, G.A. Lodygensky, F. Cicoira, Self-healing, stretchable, and highly adhesive hydrogels for epidermal patch electrodes, Acta Biomater. 139 (2022) 296–306.
[47] G. Hu, X. Lan, B. Peng, J. Liao, Y. Xiong, Water resistant, biodegradable and flexible corn starch/carboxymethyl cellulose composite film for slow-release fertilizer coating materials, Int. J. Biol. Macromol. 260 (2024) 129476.
[48] A.K. Rana, V.K. Gupta, P. Hart, F. Scarpa, V.K. Thakur, Sustainable MXene-chitosan/chitin composites for Interdisciplinary applications in water purification, bio-medical, bio-sensing and electronic fields, Mater. Today Sustain. (2024) 100671.
[49] M. Beg, J. Saju, K.M. Alcock, A.T. Mavelil, P.R. Markapudi, H. Yu, L. Manjakkal, Biodegradable biopolymers for electrochemical energy storage devices in a circular economy, RSC Sustain. (2025).
[50] L. Zhao, Y. Li, M. Yu, Y. Peng, F. Ran, Electrolyte-wettability issues and challenges of electrode materials in electrochemical energy storage, energy conversion, and beyond, Adv. Sci. 10 (17) (2023) 2300283.
[51] R. Taurino, S. Caporali, F. Borgioli, E. Galvanetto, Development and characterization of chitosan hybrid coatings by sol-gel method, XVII Convegno Naz. Aim. (2023) 193, accesso ONLINE all'editore2023.
[52] H. Yang, N. Wu, Ionic conductivity and ion transport mechanisms of solid-state lithium-ion battery electrolytes: a review, Energy Sci. Eng. 10 (5) (2022) 1643–1671.
[53] B.B. Patowary, D. Brahma, A. Mondal, Study of RuO2-and MnO2-based electrode materials and their performance review in conjunction with PANi for supercapacitor applications, Ionics 31 (1) (2025) 67–115.
[54] P. He, J.H. Park, Y. Jiao, R. Ganguli, Y. Huang, A. Lee, C.H. Ahn, M. Wang, Y. Peng, Y. Long, High-voltage water-scarce hydrogel electrolytes enable mechanically safe stretchable Li-ion batteries, Sci. Adv. 11 (15) (2025) eadu3711.
[55] L. Cui, W. Wang, J. Zheng, C. Hu, Z. Zhu, B. Liu, Wide-humidity, anti-freezing and stretchable multifunctional conductive carboxymethyl cellulose-based hydrogels for flexible wearable strain sensors and arrays, Carbohydr. Polym. 342 (2024) 122406.
[56] Y. Liu, X. Huang, J. Zhou, C.K. Yiu, Z. Song, W. Huang, S.K. Nejad, H. Li, T. H. Wong, K. Yao, Stretchable sweat-activated battery in skin-integrated electronics for continuous wireless sweat monitoring, Adv. Sci. 9 (9) (2022) 2104635.
[57] Z. Zhou, W. Zhang, Y. Zheng, Y. Yang, B. Wei, C. Liu, J.-L. Lan, C.-W. Nan, Y.-H. Lin, Advances in n-type Bi2O2Se thermoelectric materials: progress and perspective, Mater. Today Phys. 39 (2023) 101292.
[58] Y. Xu, X. Xu, M. Guo, G. Zhang, Y. Wang, Research progresses and challenges of flexible zinc battery, Front. Chem. 10 (2022) 827563.
[59] Z. Zhu, S. Xiong, J. Li, L. Wang, X. Tang, L. Li, Q. Sun, Y. Shi, J. Shao, Hydrogel polymer electrolytes for aqueous zinc-ion batteries: recent progress and remaining challenges, Batteries 11 (10) (2025) 380.
[60] X. Huang, Y. Liu, J. Zhou, S.K. Nejad, T.H. Wong, Y. Huang, H. Li, C.K. Yiu, W. Park, J. Li, Garment embedded sweat-activated batteries in wearable electronics for continuous sweat monitoring, npj Flex. Electron. 6 (1) (2022) 10.
[61] G. Liu, M. Alomari, B. Sahin, S.E. Snelgrove, J. Edwards, A. Mellinger, T. Kaya, Real-time sweat analysis via alternating current conductivity of artificial and human sweat, Appl. Phys. Lett. 106 (13) (2015).
[62] H. Yu, J. Sun, Sweat detection theory and fluid driven methods: a review, Nanotechnol. Precis. Eng. 3 (3) (2020) 126–140.
[63] J. Min, J. Tu, C. Xu, H. Lukas, S. Shin, Y. Yang, S.A. Solomon, D. Mukasa, W. Gao, Skin-interfaced wearable sweat sensors for precision medicine, Chem. Rev. 123 (8) (2023) 5049–5138.
[64] L.B. Baker, Sweating rate and sweat sodium concentration in athletes: a review of methodology and intra/interindividual variability, Sports Med. 47 (1) (2017) 111–128.
[65] D. Bol, J.D. Vos, C. Hocquet, F. Botman, F. Durvaux, S. Boyd, D. Flandre, J.D. Legat, SleepWalker: a 25-MHz 0.4-V Sub- mm2 7- μW/MHz microcontroller in 65-nm LP/GP CMOS for low-carbon wireless sensor nodes, IEEE J. SolidState Circuits 48 (1) (2013) 20–32.
[66] H. Liu, X. Ji, Z. Guo, X. Wei, J. Fan, P. Shi, X. Pu, F. Gong, L. Xu, A high-current hydrogel generator with engineered mechanoionic asymmetry, Nat. Commun. 15 (1) (2024) 1494.
[67] L. Li, Y. Shao, L. Jia, Z.H. Guo, Z. Li, Z.L. Wang, X. Pu, A d33 piezoionic hydrogel with bioinspired multi-gradient structure for enhanced mechano-iontronic transduction, Nano Energy 133 (2025) 110477.
[68] D. Das, M. Dutta, M.L. Cervera, M. de la Guardia, Recent advances in on-line solid-phase pre-concentration for inductively-coupled plasma techniques for determination of mineral elements, TrAC Trends Anal. Chem. 33 (2012) 35–45.
[69] Z. Zhang, Z. Yang, Z. Zhao, Y. Liu, C. Wang, W. Xu, Multimodal deep-learning framework for accurate prediction of wettability evolution of laser-textured surfaces, ACS Appl. Mater. Interfaces 15 (7) (2023) 10261–10272.
[70] D. Sun, A.J. Onyianta, D. O'Rourke, G. Perrin, C.M. Popescu, L.H. Saw, Z. Cai, M. Dorris, A process for deriving high quality cellulose nanofibrils from water hyacinth invasive species, Cellulose 27 (7) (2020) 3727–3740.

[71] L. Wågberg, G. Decher, M. Norgren, T. Lindström, M. Ankerfors, K. Axnäs, The build-up of polyelectrolyte multilayers of microfibrillated cellulose and cationic polyelectrolytes, Langmuir 24 (3) (2008) 784–795.
[72] W. Dang, L. Manjakkal, W.T. Navaraj, L. Lorenzelli, V. Vinciguerra, R. Dahiya, Stretchable wireless system for sweat pH monitoring, Biosens. Bioelectron. 107 (2018) 192–202.
[73] L. Manjakkal, A. Pullanchiyodan, N. Yogeswaran, E.S. Hosseini, R. Dahiya, A wearable supercapacitor based on conductive PEDOT:PSS-coated cloth and a sweat electrolyte, Adv. Mater. 32 (24) (2020).